Chapter 8

Computational Fluid Dynamics (CFD) Applied to a Glass Vaporization Chamber for Introduction of Micro- or Nano-Size Samples into Lab-Based ICPs and to a CFD-Derived (and Rapidly Prototyped Via 3D Printing) Smaller-Size Chamber for Portable Microplasmas

Hamid R. Badiei, Gordon Stubley, Ryan Fitzgerald,
Melanie Saddler and Vassili Karanassios

Additional information is available at the end of the chapter

http://dx.doi.org/10.5772/intechopen.72650

Abstract

Computational fluid dynamics (CFD) is used extensively in many industries ranging from aerospace engineering to automobile design. We applied CFDs to simulate flows inside vaporization chambers designed for micro- or nano-sample introduction into conventional, lab-based inductively coupled plasmas (ICPs). Simulation results were confirmed using smoke visualization experiments (akin to those used in wind tunnels) and were verified experimentally using an ICP-optical emission spectrometry (ICP-OES) system with a fast-response photomultiplier tube (PMT) detector, an ICP-OES system with a slower-response charge injection device (CID) detector, and an ICP-mass spectrometry (ICP-MS) system. A pressure pulse (defined as a momentary decrease of the optical emission intensity of ICP background) was not observed when employing widely used ICPs either with a CID detector or with ICP-MS. Overall, the simulations proved to be highly beneficial, for example, detection limits improved by as much as five times. Using CFD simulations as a guide, a rapidly prototyped, 3D-printed and smaller-size vaporization chamber (a scaled-down version of that used with ICPs) is being evaluated for potential use with a portable, battery-operated microplasma. Details are provided in this chapter.

Keywords: computational fluid dynamics, CFD, near-torch vaporization, NTV, ICP-OES, ICP-MS, microplasma, 3D printing, rapid prototyping

1. Introduction

According to Collins English dictionary, computational fluid dynamics (CFD) is "the prediction of the behavior of fluids and other effects of fluid motion past objects by numerical methods rather than experiments." In general terms, CFD simulations use computations based on applied mathematics and (primarily) physics to compute mass transfer, heat transfer, or fluid flow (e.g., a liquid or a gas) constrained by surfaces. It then uses computer graphics and visualization software to display the result of the computations. This way a **simulation** (i.e., a replica (or imitation) of the process being simulated over time) is obtained. Simulations can be used as research tools to predict fluid flow or to obtain insights under defined conditions (e.g., flow of air around an airplanes' wing). They can also be used as design tools to reduce the number of candidate prototypes to be evaluated before a final, experimentally verified design is fabricated. Experimental verification of simulations is often done using smoke experiments (e.g., in a wind tunnel), and this is followed by validation of prototypes (e.g., a test flight).

We used CFD simulations for rational development of vaporization chambers intended for use in elemental analysis of micro- or nano-size samples. One chamber was developed for sample introduction into a lab-size inductively coupled plasma (ICP), which is formed on the top part of an ICP torch and a CFD-derived chamber, smaller version of it for use with a portable, battery-operated, and small-size microplasma.

2. Micro- or nano-sample introduction into ICPs

Why sample introduction? Introduction of an initially ambient temperature sample into a gas-phase plasma (**Figure 1**) is the "Achilles' heel" of ICP spectrometry. Liquid samples are typically introduced into an ICP using a nebulizer requiring ~2 mL/min of sample and with <5% efficiency. Due to poor sample introduction efficiency, detection limits are impaired, and waste disposal issues are created, and due to the requirement for relatively large volumes of sample, micro- or nano-amounts of sample cannot be used.

Why elemental analysis of micro- or nano-samples? In many analytical situations, there is little sample available for analysis, for example, samples of bio-origin (e.g., metalloenzymes, constituting over 30% of all enzymes in the human body). Other examples include samples of clinical origin (e.g., lead (Pb) in the blood, every child in the USA must have Pb concentrations in their blood measured), forensics (e.g., for criminal activity investigations), and samples of interest to nanoscience and nanotechnology (e.g., due to costs involved in making large amounts of nanomaterials). Primarily due to small sample size, introduction of such samples by pneumatic nebulization (**Figure 1**) cannot be used.

How to introduce micro- or nano-samples into lab-size plasma? To replace the nebulizer/spray-chamber combination (**Figure 1**) and to enable micro- or nano-sample analysis capabilities, we have been developing and characterizing an electrothermal, near-torch vaporization (NTV) sample introduction system. An illustration of the NTV system as used by an ICP is shown in **Figure 2**.

http://dx.doi.org/10.5772/intechopen.72650

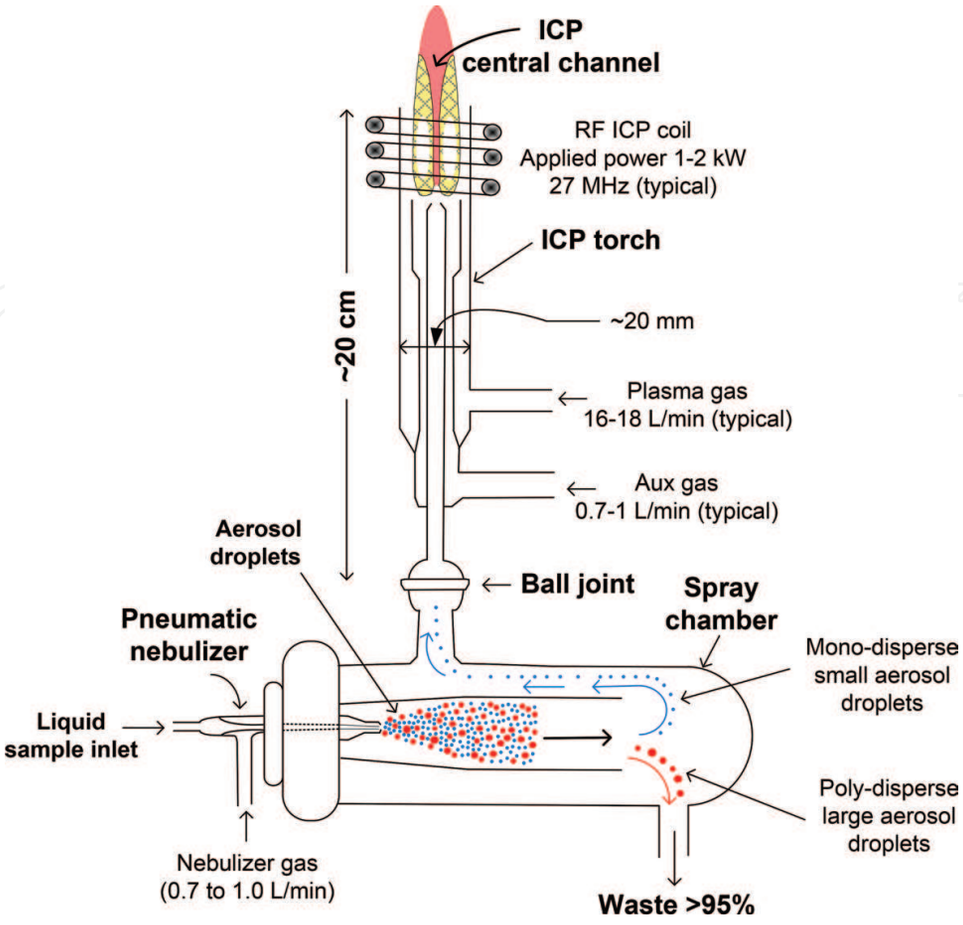

Figure 1. Nebulizer/spray-chamber combination for liquid sample introduction into an ICP torch.

Briefly, the NTV sample introduction system (**Figure 2a**) consists of a vaporization chamber that clips onto any ICP torch with a ball joint (**Figure 1**) and a coil filament made out of rhenium (Re) filament [1–5]. The coil filament is attached to a support rod. Power transfer cables running through the support connect the coiled filament to an external power supply. To deposit a liquid micro- or nano-size sample, the support rod with the coil secured to it is retracted from the vaporization chamber, an aqueous sample is pipetted onto the coil, and the support-rod coil combination with a liquid sample on the coil is reinserted into the chamber. Using an external power supply, low electrical power (e.g., <1 W) is applied to the coil, thus bringing its temperature to about 100°C, and as a consequence drying the liquid sample on the coil. Subsequently, higher electrical power is applied to the coil (e.g., ~50 W), thus raising the temperature of the coil to ~2000°C (or more, depending on applied power). At such temperatures, the dried sample residue that remained on the coil after drying is vaporized, and the vaporized sample is carried to an ICP by the carrier gas where it becomes gas-phase atoms; it gets excited (and/or ionized).

As illustrated in **Figure 2a**, when the support rod is inserted into the vaporization chamber, a seal is formed at the bottom of the chamber, and a vortex is formed inside the chamber. The vortex consists of a cylinder (constrained by the support rod and by the walls of the chamber) and of a cone (**Figure 2b**). In the center of the "cone," a lower-pressure zone is formed due to the vortex

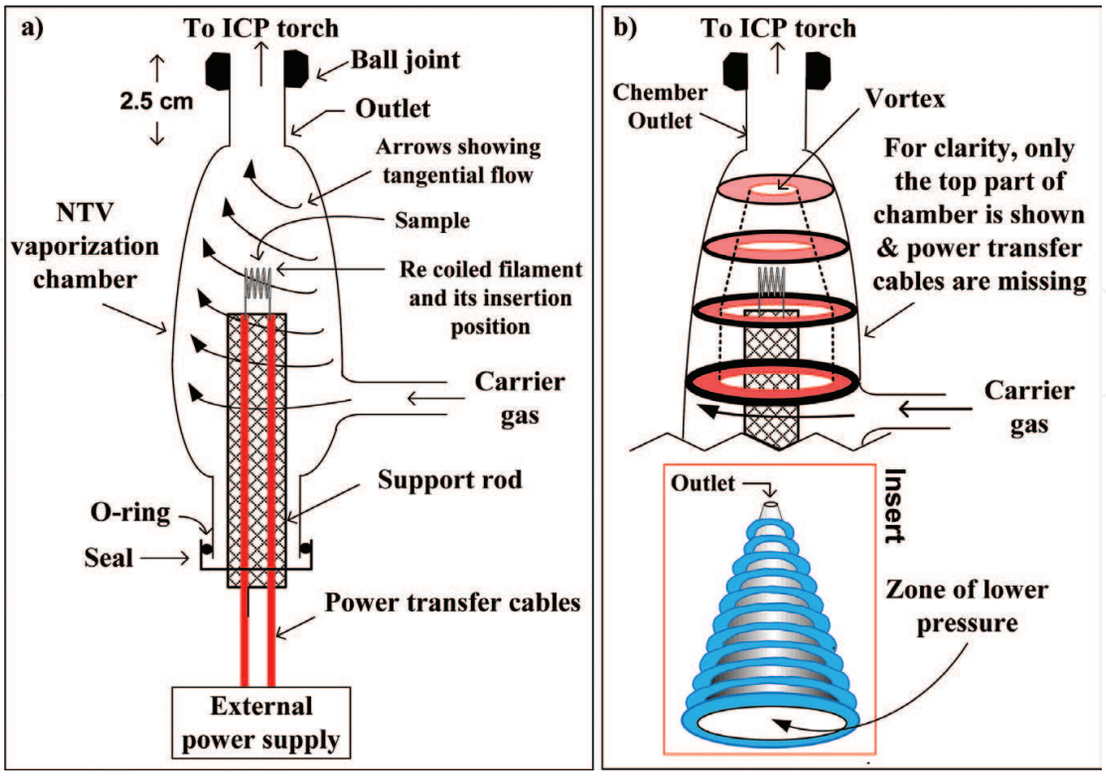

Figure 2. (a) Original, empirically designed vaporization chamber for micro- or nano-sample introduction. The ball joint allows connection to any ICP torch (**Figure 1**) with an appropriate ball joint. (b) Top part of the vaporization chamber (for clarity, only a few arrows—Representing hypothetical gas stream lines—Are shown). Insert: Hypothetical, engineered vortex-rings have been added for clarity.

(akin to an inverted vortex formed when draining a sink full of water). This way, the vaporized sample residue is kept in the center of the chamber and away from its walls (thus minimizing sample loss to the chamber walls).

Advantages of NTV (Figure 2) over a pneumatic nebulizer (Figure 1). Due to the use of relative large volumes of sample (e.g., in the mL range), a pneumatic nebulizer cannot be used for micro- or nano-sample introduction into an ICP. Also, due to its poor sample introduction efficiency (<5%), a nebulizer generates a significant amount of potentially hazardous waste (e.g., unused sample containing contaminants). NTV uses micro- or nano-amounts of sample, thus making waste disposal a nonissue. Furthermore, due to the high sample introduction efficiency of NTV (>80%), detection limits (defined as the minimum amount or concentration that can be detected with a stated statistical confidence) improve by a factor of 16 (or more) over those obtained using a nebulizer. Furthermore, although absolute-unit detection limits (pg or pictogram) do not change with volume, those expressed in relative concentration units (e.g., parts per billion or ppb) do. For instance, by changing sample volume from 5 μL to 50 μL, concentration detection limits improve by factor of 10. Experimental verification of this is provided in Section 8.3. Getting back to this ample, an overall improvement of detection limits of 160 (over those obtained with a nebulizer) can be realized. In chemical analysis, detection limits are a significant consideration and are considered by many as the key figure of merit.

http://dx.doi.org/10.5772/intechopen.72650

Comparison of NTV with its main competitor. Electrothermal vaporization (ETV) from graphite supports is the main competitor to NTV for micro-sample introduction into ICPs. Absolute amount (in pg) detection limits are compared in **Table 1** (for ICP-optical emission spectrometry or ICP-OES). From these data, it can be concluded that NTV does equally as well as the best ever reported detection limits for ETV for Zn, Pb, and Cd and that it outperforms ETV for all other elements tested (e.g., Ca, Ba, Be, Mg, V). For Ca (with NTV-ICP-OES detection limits in the millions of atoms), NTV outperforms ETV by 10,000 times [3]. Clearly, NTV is worthy of further investigation, in this case, using CFD simulations for a rational (rather than empirical) design of a vaporization chamber.

Nature of emission signals generated by NTV sample introduction. An example transient signal obtained by pipetting a Pb-containing liquid sample (100 nL) onto the Re coil, by drying it (e.g., by applying 0.3 W for 2 min to the coil) and by rapidly vaporizing the dried sample residue that remained on the coil (by applying 25 W) and by monitoring the Pb 220 nm spectral line is shown in **Figure 3a**. The transient signal (**Figure 3b**) must be digitized using a relatively fast data acquisition rate (e.g., 100 Hz).

The pressure pulse is due to a momentary expansion of the carrier gas inside the sealed vaporization chamber (**Figure 2**) caused by the rapidly heated coiled filament (with a maximum heating rate of ~6000 °C per s). As the carrier gas expands, its flow rate increases. This momentary increase in flow rate is cooling the central channel of the ICP (**Figure 1**), thus decreasing plasma background emission intensity (and hence the dip in intensity shown in **Figure 3a**). The intensity depends on ICP power (e.g., ranging from 1 to 2 kW), on the wavelength monitored (as background intensity increases from 200 to 400 nm) and on the electrical power level applied to the coil. Electrical power applied to the coil translates to temperature of the coil, for example, from 25 W (~1800°C) to 60 W (~2750°C).

Would the pressure pulse complicate CFD simulations? To address this question, the pressure pulse was studied using experimental conditions that amplify significantly the intensity of the

Element	Wavelength (nm)	Detection limit (pg)	
		NTV (5 μL)	ETV (5 μL)
Zn	213.856	0.8	0.6–800
Pb	220.353	4	4–6500
Cd	228.802	0.8	1–600
Mg	279.553	0.03	0.1–5
V	309.311	0.09	5.9–2000
Be	313.042	0.09	5.9–2000
Ca	393.366	0.0003	15
Ba	455.403	0.07	0.3–0.5

Table 1. Comparison of detection limits between NTV-ICP-OES and ETV-ICP-OES [3].

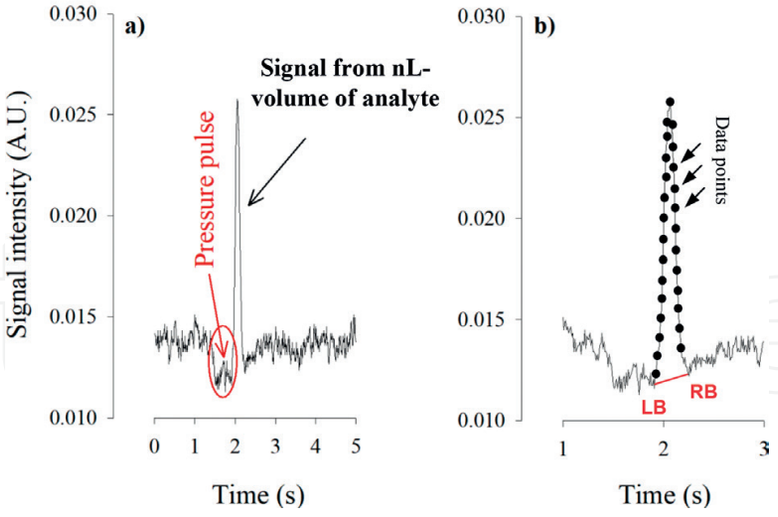

Figure 3. (a) Transient Pb signal: A momentary dip in plasma background intensity (a.k.a., a pressure pulse) is shown encircled. (b) Same as (a) but with the time axis expanded to show where the left background (LB) and right background (RB) correction points should be set for net peak height measurement or for net peak area integration. Filled circles show acquired data points (data were acquired for the entire duration of the signal; for clarity only a few points are shown).

pressure pulse (**Figure 4**). Lead (Pb) was monitored using the 220 nm spectral line, and it was chosen due to its high volatility (thus requiring a relatively low vaporization power of 25 W) and due to its low emission wavelength (where plasma background emission intensity is low).

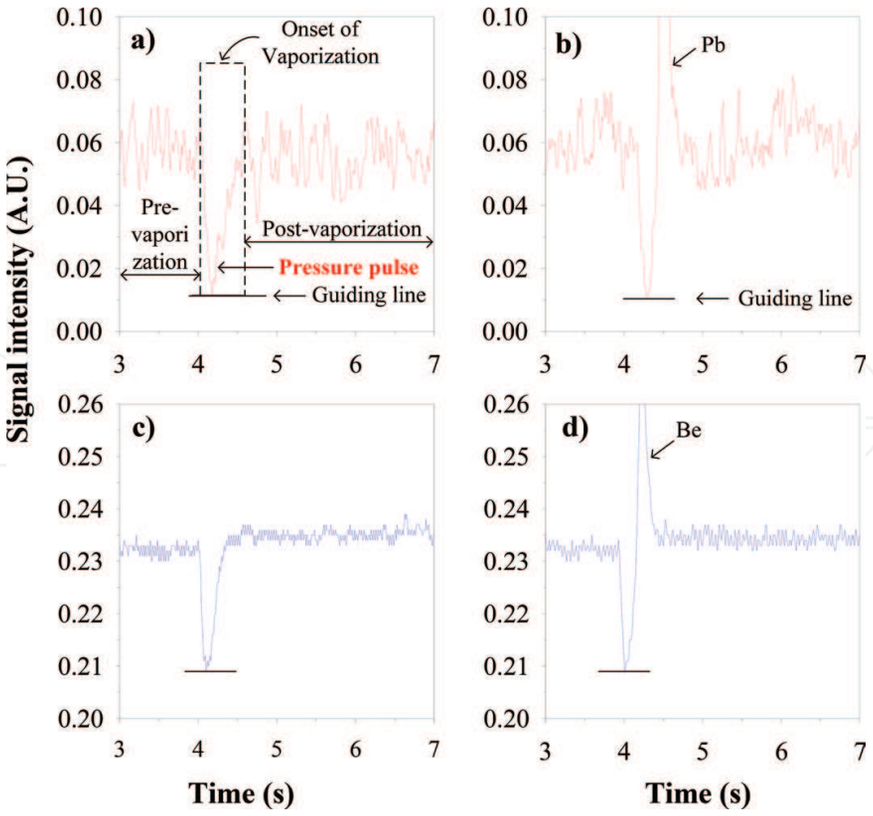

Figure 4. Transient signals obtained by running water blanks or Pb or Be (beryllium) analytes (i.e., the chemical species of interest). (a) Water blank at 220 nm and (b) a signal from a Pb (at 220 nm). And (c) signal obtained from a water blank at 313 nm and (d) from Be (at 313 nm).

Beryllium (Be) was selected due to its low volatility (thus requiring a relatively high vaporization power of 60 W) and its higher emission wavelength (at 313 nm, where plasma background emission intensity is higher than it is for Pb).

To facilitate discussion, the signal in **Figure 3a** is subdivided into three segments: a pre-vaporization event (with no electrical power applied to the coil), a vaporization event (with power applied to the coil), and a post-vaporization event (with continuous application of power for 10 s, the x-axis has been expanded for clarity). Thus, information about plasma emission is obtained before, during, and after vaporization.

For both Pb and Be (**Figure 4b** and **d**), the pre-vaporization plasma emission intensity has the same magnitude as the post-vaporization. However, for Be (**Figure 4c** and **d**), the post-vaporization background intensity did not return to its pre-vaporization level. There are two likely reasons for this. One, as the heated carrier gas reaches the ICP, some plasma energy is freed up (i.e., energy that would otherwise have been used to heat the carrier gas); thus background emission intensity increases. And two, some light emitted in the visible range of the spectrum by the glowing Re coil enters the spectrometer. However, background correction is not affected. As a sample starts to vaporize, the width of the pressure pulse decreases, but this is compensated for by setting the proper background correction points (**Figure 3b**). From these observations and from the observed linearity of calibration curves for many elements, it can be concluded that there is no need to take into consideration the pressure pulse in the CFD simulations.

3. Experimental: Using an ICP-OES system in a lab

An optical ICP spectrometer with a **fast-response p**hoto**m**ultiplier **t**ube (**PMT**) detector was mainly used (**Figure 5**) [2]. This spectrometer was selected due the sensitivity of the PMT and because transient signals can be acquired simultaneously from several PMT channels at 100 Hz, thus making it ideal for transient signals and for the study of a pressure pulse. It should be noted that faster heating rates and higher vaporization powers applied to the coil (corresponding to vaporization temperatures) generally translate to taller peak heights, to better **s**ignal-to-**n**oise **r**atios (**SNRs**) and to improved detection limits. They also translate to **a more intense pressure pulse**.

4. Fate of analytes in the chamber during vaporization

The phenomena taking place immediately after vaporization of a dried sample residue on a coil are influenced by the design of the vaporization chamber and by gas-flow dynamics. These can be grouped into two categories: the physical/chemical properties of the **analyte** (defined as chemical species of interest) and the sample's **matrix** (defined as whatever the analyte is in) and the processes that take place as the vaporized sample travels from the top of the coil to the outlet of the chamber.

To generalize [6–10] and unless an element (or a compound) of interest in the dried sample residue on the coil sublimes, to be vaporized, the solid residue must first become a liquid. As

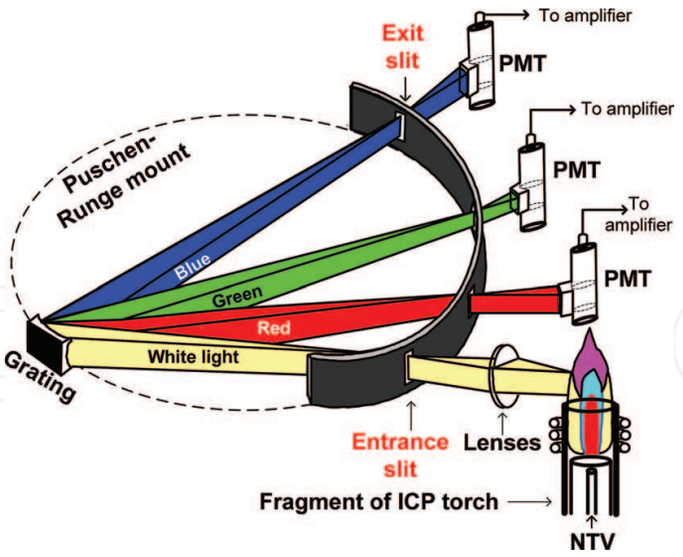

Figure 5. PMT-based, simultaneous optical spectrometer. See text for discussion.

the temperature of the coil increases, the residue first becomes a liquid, and then the liquid is vaporized. Nucleation takes place in the gas phase; the vapor condenses forming a particle-loaded aerosol with a critical particle diameter d_p. The value of d_p depends on parameters such as surface tension of the liquid droplet (σ), the molecular volume of the vapor species (V_m), the temperature (T, in Kelvin), and the saturation ratio (S). These parameters are related by the following equation (Eq. (1), where, k is the Boltzmann constant):

$$d_p = 4\sigma \frac{V_m}{k \cdot T \cdot \ln S} \tag{1}$$

The saturation ratio (S) is a measure of analyte supersaturation and is determined by dividing the partial vapor pressure p_{vap} (in atm) of the analyte of interest by the value of the equilibrium vapor pressure of a particular species at the temperature of nucleation (Eq. (2)):

$$S = \frac{p_{vap}}{p_{(T)}} \tag{2}$$

As the temperature of the surface of the Re coil increases and the analyte begins to vaporize, the partial pressure p_{vap} of an analyte in the carrier gas also increases. This can be estimated using the following equation (Eq. (3)):

$$p_{vap} = \frac{N_s \cdot T_g \cdot R}{V_g \cdot t_v} \tag{3}$$

where N_s is the number of moles of vapor from the evaporated sample, T_g is the initial temperature of the carrier gas, R is the gas constant, V_g is the flow rate of the carrier gas at T_g, and t_v is the mean evaporation time of the main portion of the sample.

From these equations it can be inferred that as the partial vapor pressure of the analyte (p_{vap}) increases (by increasing the temperature of the coil), the saturation ratio (S) also increases (Eq. (2)). Therefore, the critical diameter (d_p) of condensed particles in the aerosol shifts to smaller diameters (Eq. (3)), and as a result, the concentration of analyte particles (e.g., the number of particles per unit volume) increases.

Once an aerosol has been formed on top of the coil, a set of forces inside the chamber determine both particle size and fate of particles as they travel inside the chamber toward its outlet. For example, under the influence of a temperature gradient in the carrier gas (which is hotter closer to the coil and cooler on the chamber walls), particles in the aerosol tend to move toward the lower temperature region of the chamber. This phenomenon is known as *thermophoresis* (or *thermomigration*) [11–13]. Thermophoresis causes dispersion (i.e., causing a plug of aerosol to become wider), thus moving particles from the center of the chamber (ideally where they should be) toward the walls of the chamber (and may even be causing particle adhesion to the walls of the chamber thus possibly causing sample losses).

5. Toward an ideal vaporization chamber

From the foregoing it can be concluded that an **ideal** vaporization chamber prevents dilution (in the gas phase) of a vaporized sample inside the chamber by keeping the analyte (as much as possible) in the center of the chamber. This also reduces adhesion of vaporized particles on the walls to the chamber (thus reducing analyte loss). Narrower and shorter plugs of analyte (i.e., narrower spatially and shorter temporally) also minimize diffusion and thermomigration (both of which are time-dependent). In general, narrower and shorter plugs of vaporized sample generate sharper and more intense signals for the same amount of sample. Generally, more intense signals translate into improved detection limits.

From a practical point of view, geometrical simplicity of a vaporization chamber is an asset, at least from the point of view of its fabrication using a glassblower. For example, the original design was empirical (**Figure 2a**) and admittedly rather difficult to reproduce (from an exact geometrical shape and dimensions' point of view). Thus, an **ideal** chamber should have a well-defined and easy-to-reproduce geometry. An example of such a chamber is shown in **Figure 6**.

The "ideal" chamber (**Figure 6**) consists of a cone sitting on top of a cylindrical barrel. This design is akin to an inverted dust-sorting cyclone with well-defined dimensions. From the

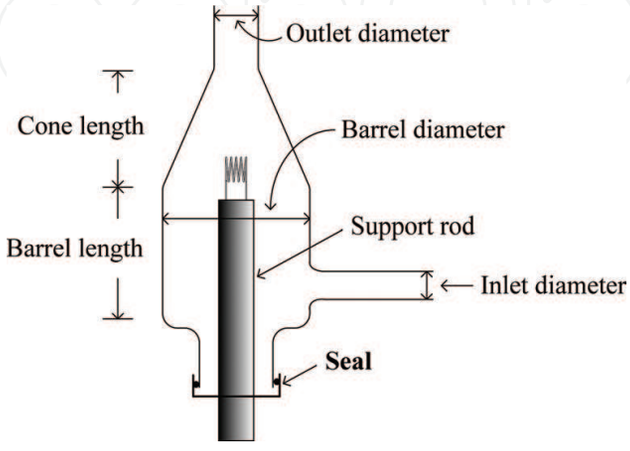

Figure 6. "Ideal" vaporization chamber. Dimensions are missing because they were decided based on the results of the simulations (as will be discussed in a later section). Power transfer cables running through the support rod and the external power supply have been omitted for simplicity.

practical point of view, glassblowing such an ideal chamber with reproducible and well-defined dimensions is easier to fabricate than an empirical one (**Figure 2**). Similar types of arguments apply to simulations.

6. Computational fluid dynamics for an ideal chamber

In simple terms, the key idea behind CFD is to use a computer to simulate fluid-flow, heat-transfer, and associated phenomena. At present, CFD simulations have found applicability in multibillion dollar-a-year industries, including automobile, aircraft, and aerospace. In this case, vaporization chambers can be "designed" and "tested" on a computer screen before being fabricated (typically by a manual, glassblowing process) and prior to being tested by an (expensive to purchase and operate) ICP.

The physical aspects of fluid flow are governed by three fundamental principles: conservation of mass (continuity equation), conservation of momentum (Navier–Stokes equations), and conservation of energy. These principles are described by partial differential equations and have been described elsewhere [14–20], so they will not be repeated. Computational fluid dynamics discretizes and replaces the differential equations by algebraic equations so that numerical solutions can be computed. The CFD software we used was originally developed in Waterloo, Canada, and it is now available from ANSYS Corp.

6.1. Steps required for simulation of an NTV chamber

There are three basic steps to a simulation: preprocessing, numerical solutions of equation (e.g., using a solver), and postprocessing. These will be discussed in conjunction with an NTV chamber.

6.2. Preprocessing

In preprocessing, the flow pattern to be simulated is transformed from a diagram into a form suitable for use by software. There are several steps taking place during preprocessing. Briefly:

(a) The target geometry of the fluid-flow domain is defined in computer terms.

(b) The physical phenomena (e.g., fluid flow, heat transfer) to be modeled are selected.

(c) The fluid properties (e.g., density, viscosity) and their values are entered into the software.

(d) Appropriate boundary conditions are specified on the flow domain boundaries (e.g., walls, inlets).

(e) A grid (or mesh) is generated; an example is shown in **Figure 7**. The target geometry is subdivided into small, nonoverlapping controlled volumes or elements or subdomains (also called cells).

Profiles of gas velocity, gas pressure, and gas temperature are calculated at the nodes of each cell. The accuracy of the calculations depends on the number of cells, and the larger the number

http://dx.doi.org/10.5772/intechopen.72650

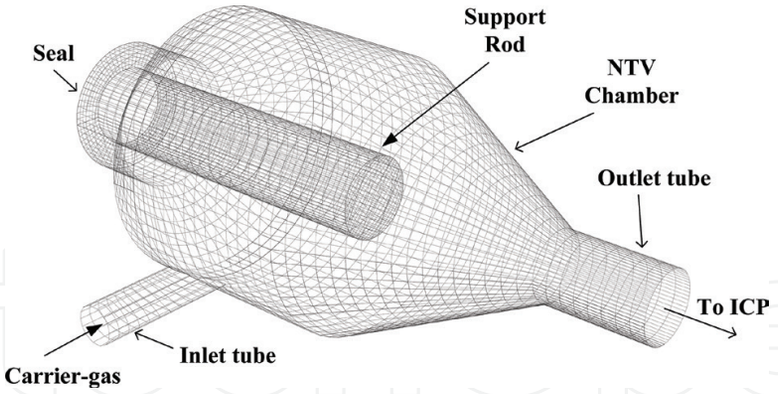

Figure 7. Meshed vaporization chamber with ~16,000 finite control volumes used for preprocessing.

of cells, the better the accuracy. But, there is a limit as to how many cells can be included, and this limit is set by the speed of the calculations and hence time and cost. A compromise number of cells were used in this project.

6.3. Numerical flow simulation using the "solver"

For the simulation, the algebraic equations are derived from the appropriate differential equations and are solved by employing an iterative method. Briefly, in the "solver" (as is called in the software used for this work), a finite volume method is used, and this involves the following steps:

(a) The equations that govern fluid flow are integrated over all finite control volumes (**Figure 7**).

(b) The algebraic equations are solved using an iterative method and an initial guess as a starting point.

(c) The iterations continue until an acceptable convergence is obtained.

In addition to the steps listed above, the operation of the solver requires the use of additional parameters. Although many of these parameters are employed using their default values, others must be explicitly set by the user. Included among them are the time step for the evolution of flow (i.e., each iteration is treated as a step forward in time), the choice of discretization scheme, and the selection of output fields. Although the focus is on steady-state simulations of fluid flow, a transient evolution is also used (as required to account for the rapidly heated Re coil). The choice of an appropriate time step is important because it dictates the rate of convergence. Good convergence was obtained when a time step was set to about 30% of the average residence time a parcel of fluid spends in the chamber. Also, the variation of gas-flow velocities and pressure inside the chamber (including flow fields between each node) were approximated to form discrete equations. These approximations are referred to as the "discretization scheme." There are different discretization schemes in the CFD software we used, the upwind differencing scheme was selected because it is suitable for highly convective flows and because it takes into consideration flow direction. In general, the solution of the algebraic

equations is the most computationally intensive. In the version of the software we used, the operation of the solver is displayed using a graphical diagnostic tool in a separate window (called the solver monitor). At the end of each simulation, the results of the solver monitoring window can be saved to a file for future reference.

6.4. Postprocessing and visualization of simulations

The postprocessor provides graphical and quantitative information of the results calculated by the "solver." Examples of data visualization tools include grids, x-y plots, vector plots, animations, and fringe plots. A color fringe plot is similar to a contour plot with each color band representing a range of values, but unlike contour plots, control over the width of each color band is not allowed. To provide readable fringe plots when using black-and-white printing, only a couple of color fringe plots have been included in this chapter. As a replacement of color fringe plots, 2D plots at two different locations in the vaporization chamber are included instead. In addition, animations are a very useful visualization tool because they provide an overall progress (over time) of the dynamics of gas flow. For this chapter, individual frames were extracted from animations and were included. The results of the simulations of the NTV chamber will be presented next, aided by some of the data visualization tools mentioned above.

6.4.1. Pressure profile

A fringe plot of the pressure profile inside the chamber and on a plane cutting through the center of the chamber along its length is shown in **Figure 8a**. A region of higher pressure is shown at the bottom of the chamber and directly opposite to the carrier-gas inlet. The simulations

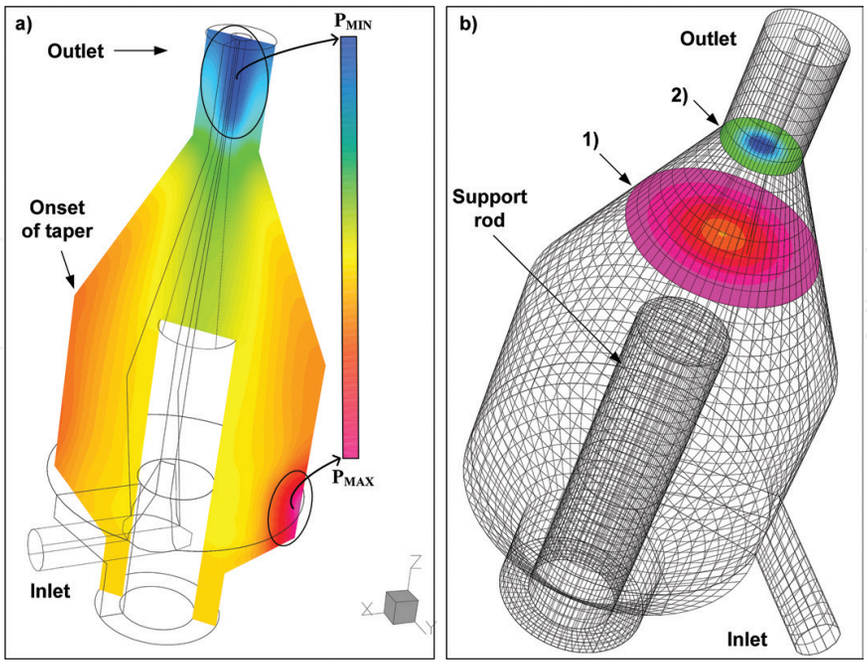

Figure 8. (a) Fringe plot of the pressure profile inside the chamber on a plane cutting through the chamber along its length (outline of chamber has been included). (b) Meshed vaporization chamber, identifying locations 1 and 2 that were used in subsequent figures.

show that there is (relatively) higher gas pressure on the walls of the chamber rather than in its center. As the chamber begins to taper (and it becomes narrower), the carrier gas generates a region of (relatively) lower pressure in the center of the chamber (as compared to the walls of the chamber). This was anticipated as shown in **Figure 2b**.

To illustrate pressure differences (important especially when using a black-and-white printed version of this work), fringe plots have been omitted, and 2D versions of pressure *versus* radial distance inside the chamber were selected for two locations (**Figure 8b**) inside the chamber. The results are shown in **Figure 9**.

The plots shown in **Figure 9** were purposely plotted using the same value for the y-axis to show the pressure drop as the chamber tapers and a vortex is formed. Using the dashed lines (**Figure 9**) as a guide, these plots reveal that pressure drops across the chamber (i.e., from the walls toward the center of the chamber) and that the pressure profiles are not ideally symmetrical. The slight asymmetry is likely due to the carrier gas being introduced only from one side of the chamber (**Figure 8**).

6.4.2. Tangential velocity profile

The 2D tangential velocity profiles are shown in **Figure 10** for the two positions identified in **Figure 8b**. As shown in **Figure 10a** (for position 1, **Figure 8b**), the gas velocity at the wall is zero. The tangential velocity then steadily increases; it reaches a maximum, and it then drops to a minimum at the center of the chamber. There is a similar trend on the other side of the chamber but in the opposite direction. Similar trend (**Figure 10b**) was observed for position 2 (**Figure 8b**). In contrast to the data shown in **Figure 10a**, for the data shown in **Figure 10b**, there is an increase in the absolute magnitude of the tangential velocity as the carrier gas flows through the conical part of the chamber (**Figure 8**). In this case, to maintain a constant volumetric flow rate, the tangential gas velocity must increase as the diameter of the chamber decreases. The tangential velocity profiles for either side of the central axis of the chamber are not identical, likely due to the asymmetric introduction of carrier gas to the chamber through one inlet (**Figure 8**).

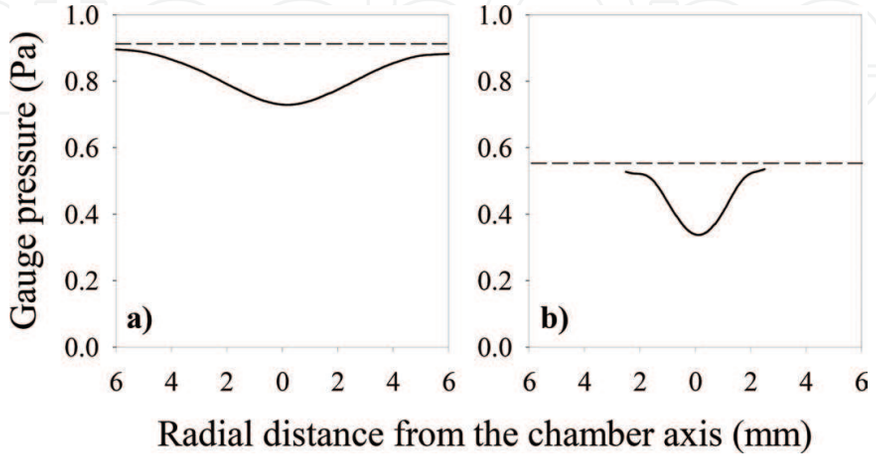

Figure 9. Pressure *versus* radial distance across the chamber's central axis at two cross sections. (a) At 20 mm from the carrier-gas inlet (1 in **Figure 8b**) and (b) at the base of the outlet (2 in **Figure 8b**).

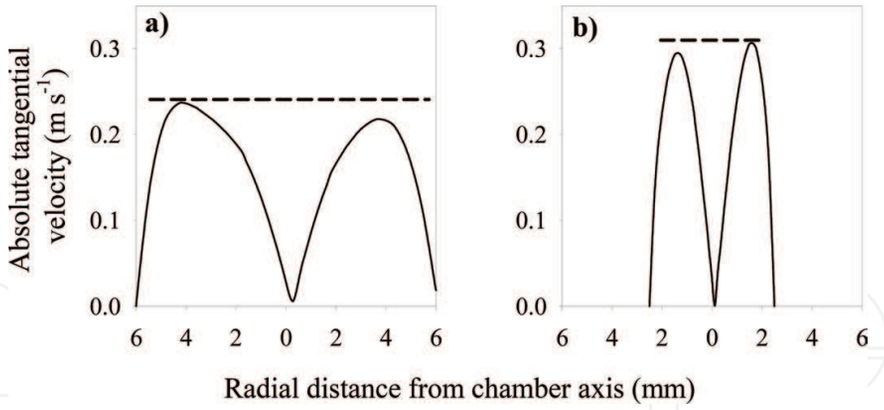

Figure 10. Tangential velocity *versus* radial distance from the chamber axis at two cross sections (**Figure 8b**). (a) At 20 mm above the carrier-gas inlet and (b) at the bottom of the chamber's outlet. The dash lines have been added to facilitate comparisons.

6.4.3. Radial velocity profile

Figure 11 shows radial velocity. This is a vector in the x direction (**Figure 8a**) and is a result of a pressure gradient; it is similar to **Figure 10**, and it is primarily responsible for keeping the analyte in the center of the chamber. As expected, the magnitude of the radial velocity (**Figure 11**) increased as the carrier gas reached the smaller diameter of the chamber. A max radial velocity was observed (at almost) the mid-distance between the wall and the center of the chamber. Imbalances in the magnitude of radial velocity on both sides of the chamber (**Figure 11**) have been observed, and these likely cause the vaporized analyte to be driven slightly away from the center of the chamber and thus somewhat disperse vaporized analytes.

6.4.4. Axial velocity profile

This velocity vector is in the z-direction (**Figure 8a**); it is specifically directed toward the outlet tube of the chamber, and it is responsible for carrying the vaporized analyte out of the chamber.

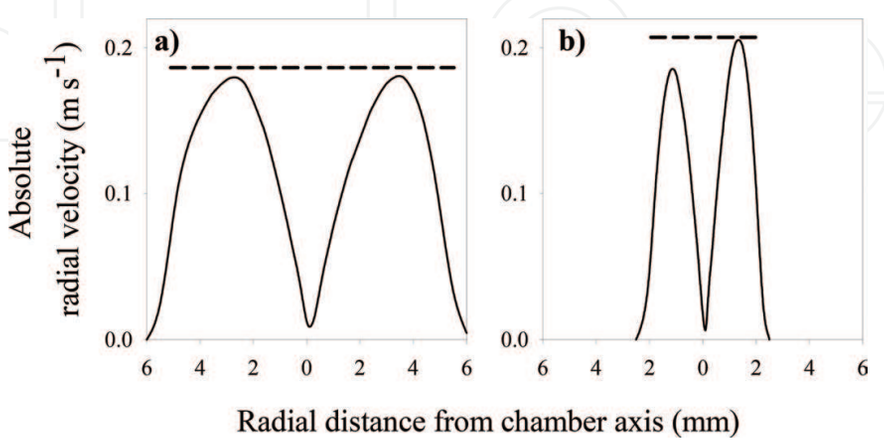

Figure 11. Radial velocity *versus* radial distance from the chamber axis at two cross sections (**Figure 8b**). (a) At 20 mm above the carrier-gas inlet and (b) at the bottom of the chamber's outlet. The dash lines have been added to facilitate comparisons.

http://dx.doi.org/10.5772/intechopen.72650

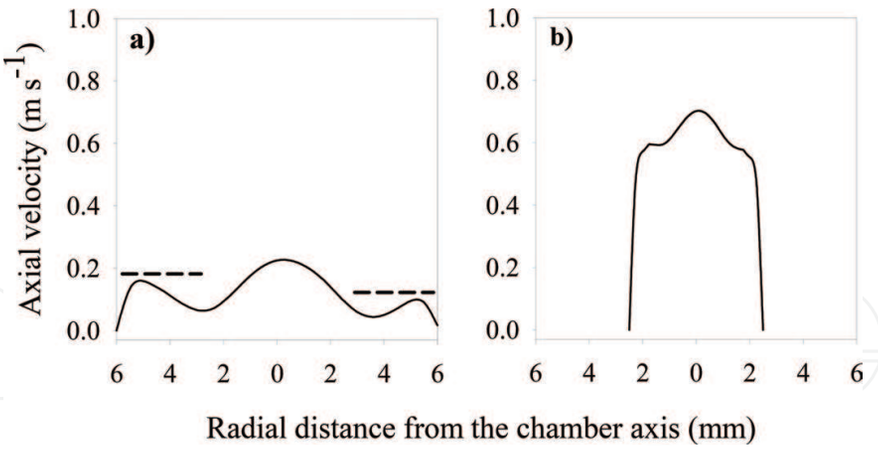

Figure 12. Axial velocity *versus* distance from the chamber axis at two cross sections. (a) At 20 mm above the carrier-gas inlet (**Figure 8b**) and (b) at the bottom of the outlet tube of the chamber. Dash lines have been included to facilitate comparisons.

As shown in **Figure 12**, axial velocity reaches a maximum at the center, and it increases as it reaches the bottom of the outlet of the chamber (**Figure 12b**). At 20 mm (**Figure 12a**), there are two distinct local minima. These are important because if a portion of vaporized analyte enters any of these regions, analyte loss could occur, and a longer (in the time domain) plug of vaporized analyte will be observed. These observations partially explain why carrier-gas-flow rate is an important parameter in NTV.

6.4.5. Streak lines

In streak lines, a fluid parcel can be tracked. Shown in **Figure 13** are two color-coded parcels of fluid (e.g., two streak lines). Streak lines can be coded to represent pressure, velocity, or time of arrival.

6.4.6. Particle tracking, the effect of insertion position, and a dual-inlet chamber design

Particle tracking permits the release (at a specific location) of a given number of particles (**Figure 14**). The properties of the particles can be set, e.g., their number, their size, their density, their temperature, and the direction of release. Particles follow the mean gas velocity, and by tracking particle position, the velocity and time of arrival at each node can also be followed. The data shown in **Figure 14** reveal the significance of insertion position, a proper insertion position (**Figure 14a**) in which particles are confined within the center of the chamber (thus producing sharp and more intense signals) and an improper insertion position (**Figure 14b**) showing particles dispersed throughout the chamber (thus producing wider signals). As mentioned, the sharper and more intense the analyte signal, the better the signal-to-noise ratio (SNR).

From the results shown in **Figure 15**, it can be concluded that by confining the analyte even more in the center of the chamber (e.g., by using a symmetrical design with a dual tangential inlet), narrower and sharper plugs of analyte would be produced at the outlet, and thus narrower and sharper signals would be measured at the detector. This has been confirmed experimentally, as will be discussed later.

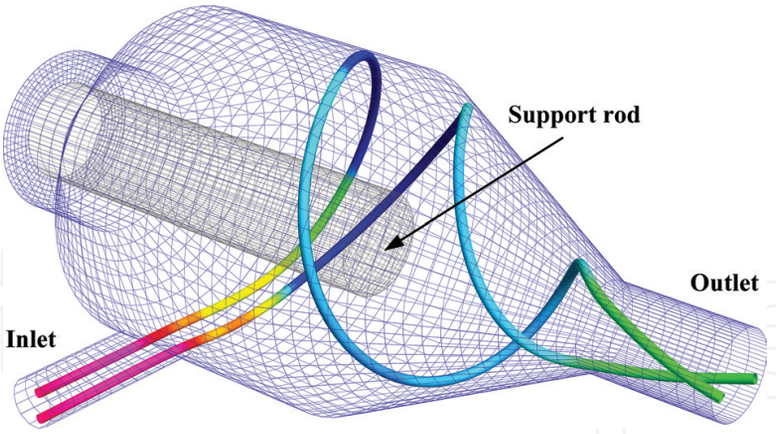

Figure 13. Two streak lines of a fluid parcel (e.g., carrier gas) are shown as they start from the inlet of the chamber, they swirl around inside the chamber, and they exit through its outlet.

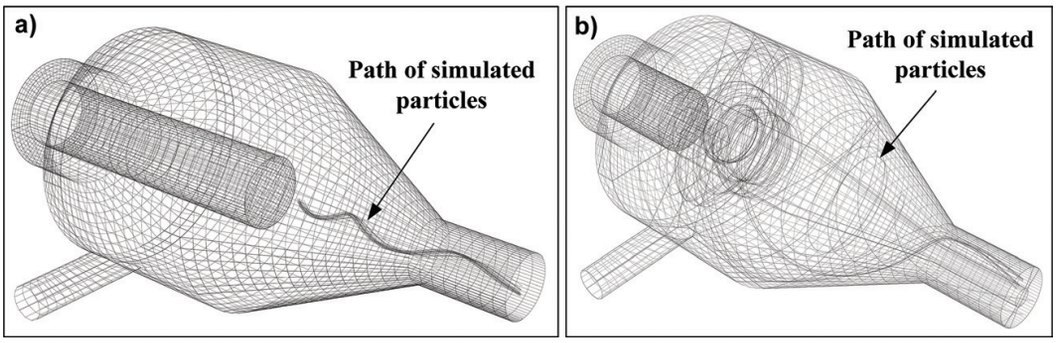

Figure 14. (a) Particles released at ~20 mm for the inlet and (b) particles released at 0 mm from the inlet.

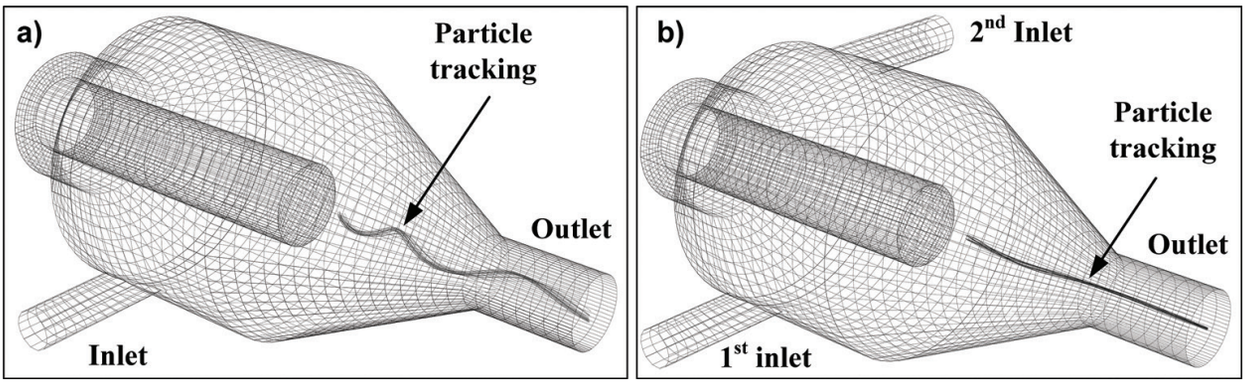

Figure 15. Comparison of two chamber designs: (a) a single-inlet chamber and (b) a dual-inlet chamber (two tangential inlets improve sample confinement within the center of the chamber).

In a separate simulation, the length of the outlet tube of a single-inlet chamber was extended from the typical ~2.5 cm (**Figure 2**) to ~17 cm, so that it would be of the same length as the inner tube of an ICP torch (**Figure 1**). This was done to examine how the extra length affects particle dispersion of vaporized plugs of analyte reaching the plasma. This simulation showed that the vortex formed inside the chamber is extinguished as the gas travels further into the (now) elongated outlet tube. Eventually, the flow becomes laminar (with a higher axial velocity at the center of this elongated tube). The bulk of the vaporized particles remains confined within

http://dx.doi.org/10.5772/intechopen.72650

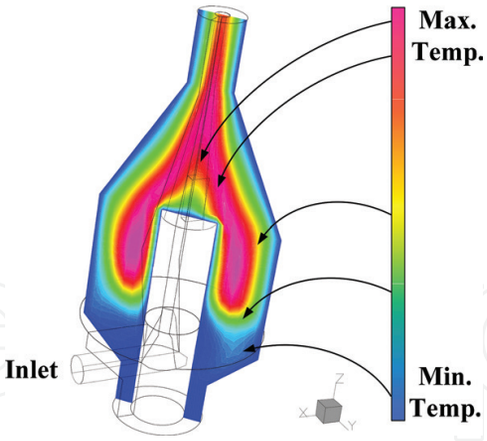

Figure 16. Fringe plot of the temperature profile on a plane cutting through the length of the chamber. An outline of the vaporization chamber has been included for guidance.

the center of the tube. However, the size of the vaporized plug increased by about 50%, thus broadening the peak measured by the detector. This simulation clearly shows that the length of the outlet tube should remain as is (**Figure 2**) and should not be elongated.

6.4.7. Video animations of streak lines or of particle tracking

Video animations are powerful means of visualizing simulations because they provide visual clues on how a gas or the vaporized particles propagate through the chamber in time. The results of a simulation are animated by repeating a simulation multiple times, with each repetition incrementing a key variable (e.g., time). At the end of each simulation, a snapshot is taken, and multiple snapshots are combined (e.g., stitched) together to make a video clip. Both streak lines and particle tracking can be animated. We generated video animations; for completeness, some examples are Internet accessible [21–23].

6.4.8. Simulation of a temperature profile

Heat transfer was also simulated, and a temperature profile inside the vaporization chamber was obtained by enabling the heat-transfer feature of the software used, by setting the vaporization temperature to 2500°C and the temperature of the wall and of the supporting rod to 25°C. Two mechanisms of heat transfer were considered, namely, thermal radiation and convection. An example of a temperature profile is shown in **Figure 16**. The temperature profile shows a relatively high-temperature region below the Re coil and around the support rod. It is likely that heat from the heated coil is radiatively transferred to this region.

7. Chambers designed based on simulation results

Based on the generic design of **Figure 6**, six chambers (**Figure 17**) with varying dimensions (**Table 2**) were simulated. And guided by the results of the simulations, they were fabricated. This was done to experimentally verify the effect of dual inlet, of barrel diameter and length, and of reduced inlet diameter.

Figure 17. NTV vaporization chambers fabricated as a result of the CFD simulations. Dimensions listed in **Table 2**. A Canadian penny (a 1 cent coin) has been included for size.

From the standard deviations shown in **Table 2**, it can be concluded that the size of the particle plug has been reduced by a factor of ~4 (chambers NTV 1 *versus* NTV 6, **Figure 17**). In other words, chamber NTV6 is expected to produce narrower and sharper analyte signals, i.e., signals with an improved SNR.

Name	Barrel Dia./mm	Barrel Length/mm	Cone Length/mm	Inlet Dia./mm	No. of Inlets	Std. Dev. Time/s*
NTV1	20	15	15	3	1	4.81E-03
NTV2	20	15	15	3	2	4.11E-03
NTV3	15	15	15	3	1	3.52E-03
NTV4	20	7.5	22.5	3	2	3.68E-03
NTV5	15	7.5	22.5	3	2	1.70E-03
NTV6	15	7.5	22.5	2	2	1.15E-03

* The conditions used for the simulations and particle tracking are summarized below:

Fluid Properties
Density: 1.78 kg m^{-3}
Viscosity: 2.29E-5 Pa s
Specific heat (P): 520 J kg^{-1} $°C^{-1}$
Specific heat (V): 312 J kg^{-1} $°C^{-1}$

Boundary Conditions
- **Inflow** (steady)
Type: velocity (normal vector)
Flow rate: 0.7 L min^{-1}
- **Outflow** (steady)
Type: pressure (static, applied as face)
Pressure value: 0 Pa (gauge pressure)
- **Wall** (steady)
Type: stationary
Action: particles to reflect from walls

Solver Parameters
- Time step: 0.01 s
- Max. residual: 1.0E-5

Particle tracking
- Density: 4500 kg m^{-3}
- Average dia.: 1.0E-7 m
- Temperature: 1500°C
- Particle Emissivity: 1
- Speed: 1 m s^{-1}
- No. of particles: 200
- Release position: 20 mm from chamber inlet.

Table 2. Dimensions of the vaporization chambers designed and tested.

The last column lists the standard deviation of the time of arrival of 200 particles, as determined by the simulations.

8. Experimental verification of CFD simulations

The results of the simulations were initially evaluated using smoke experiments. Subsequently, experimentally obtained results were obtained using three ICP systems: two of them configured for optical emission spectrometry (OES) measurements and one for mass spectrometry (MS) measurements.

8.1. Experimental verification using smoke visualization experiments

Initially, visualization using smoke was used to obtain a confirmation of the results of the simulations. Smoke was generated by pipetting a drop of oil onto the coil, by applying low electrical power to the coil (thus generating smoke) and by videotaping the resulting smoke streaks inside each of the vaporization chambers (**Figure 17**). To facilitate comparisons with the simulations, the chambers used for the smoke experiments were intentionally built the same size as those used for the simulations. Example still frames extracted from corresponding videos for a single-inlet and dual-inlet chambers are shown in **Figure 18**. There is a striking similarity between the simulations (**Figure 15**) and smoke visualization results (**Figure 18**).

For all chambers tested (**Figure 17**), the in situ generated smoke "streaks" were confined within the center of each chamber. Representative examples are shown in **Figure 18**. As shown in **Figure 18a** for a single-inlet chamber, smoke swirled (following a cork-screw-like trajectory) before exiting the chamber through its outlet. For a dual-inlet chamber (**Figure 18b**), smoke streaks roughly followed a straight line from the top of the coil toward the outlet tube of the chamber. It can thus be concluded that dual-chamber designs will produce shorter and sharper signals, therefore resulting in improved signal-to-noise ratios.

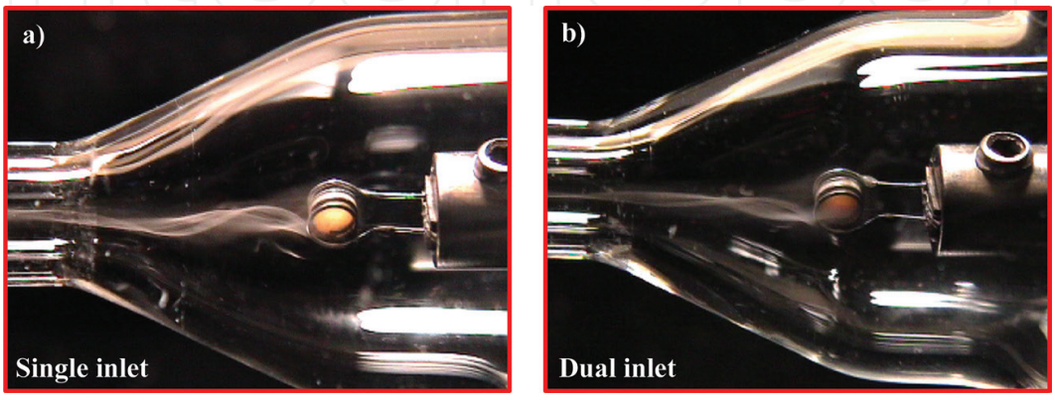

Figure 18. Example frames extracted from videos of smoke experiments. (a) Single-inlet chamber and (b) dual-inlet chamber. See text for discussion.

8.2. Experimental verification using NTV-ICP-OES with a fast-response PMT detector

An axially viewed ICP-AES system with multiple PMT detectors was used (**Figure 5**) [2]. The carrier-gas-flow rate, the coil insertion position, and the vaporization power were the same for all chambers tested (**Figure 17**). Although two elements were tested, for brevity only results for Zn are shown (**Figure 19**).

The effect of chamber design on analyte peak height and peak width is shown for Zn in **Figure 19a**. To facilitate comparisons, the same amount of analyte and the same operating conditions were used throughout (e.g., insertion position, flow rate, vaporization, and ICP power). A comparison of two chambers with otherwise similar dimensions (NTV1 and NTV 2, **Figure 17**) revealed that the chamber with a dual inlet (NTV2) showed sharper signals, thus also confirming the results of the simulations. From a comparison between the two single-inlet chambers (NTV1 and NTV3, **Figure 17**), it can be concluded that reduction of the barrel diameter (e.g., from 20 mm to 15 mm) offers an improvement in signal intensity, and it shows narrower and sharper signals. This was attributed to a higher gas velocity when using a smaller-volume chamber with the same volumetric flow rate. The last two chambers (both dual inlet, NTV5 and NTV6, **Figure 17**) showed significantly more intense signals and comparatively a smaller-intensity pressure pulse. Overall, chamber NTV6 outperformed all other chambers.

Background intensities between **Figure 19a** and **b** are different due to the use of different amplifier gains. The SNR computed using the average net intensity of the reproducibility signals (**Figure 19b**) was 156, thus making the detection limit (using the 3σ criterion) equal to an impressive 0.2 pg (or

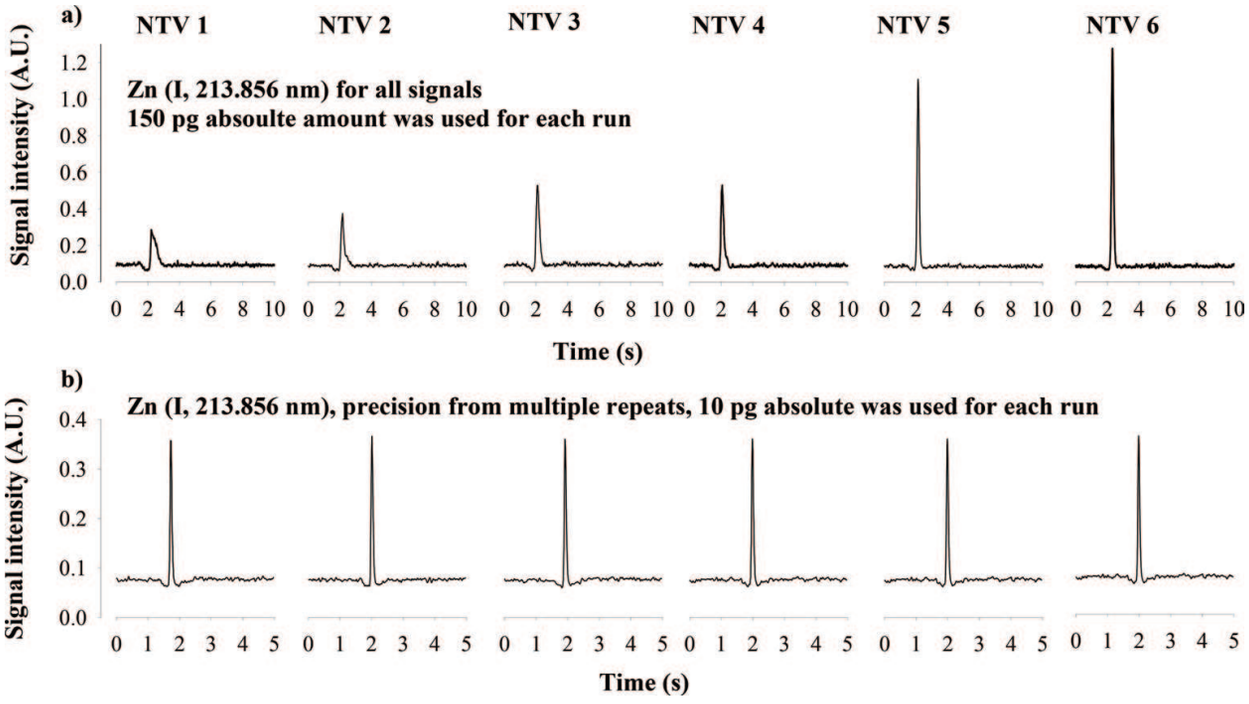

Figure 19. (a) Example signals obtained from Zn (150 pg absolute amount for each run) and for each chamber. (b) Example reproducibility using 10 pg (picogram or 10^{-12} g) of Zn (for each run) using chamber NTV6. For brevity, only the first 6 of 10 consecutive runs are shown.

0.2×10^{-12} g) or 200 femtogram (fg, or 200×10^{-15} g). Other detection limits were 0.8 pg for Pb and 0.4 pg for Cd. These improved over those listed in **Table 1** (obtained with an empirically designed chamber, **Figure 2**), for example, for Pb by ~5 times. Overall, the detection limits for Pb, Cd, and Zn are now all in the fg range (remarkable for ICP-OES). Precision was less than 2%, and this is similar to what has been reported for the empirically designed chamber. With the dual-inlet design, balancing two flows was challenging.

Overall, the results discussed above are in general agreement with the CFD simulations. The dual-inlet chamber-design-labeled NTV6 (**Figure 17**) incorporated improvements revealed during course of this work. For example, a smaller barrel diameter was used (thus reducing chamber volume and hence analyte dilution in the gas phase). The smaller diameter for the inlet tubes that was employed generated higher carrier-gas velocities; thus for the same absolute amount of analyte, plug was introduced into the ICP, and this generated higher analyte concentration per unit time. Thus taller and sharper signals were measured at the detector, and such signals generated improved SNRs and better detection limits.

Further confirmation of a potential broader utility and applicability of chamber NTV6 (**Figure 17**) was obtained by interfacing this chamber to two other ICP spectrometers: one with a charge injection device (CID) detector and the other an ICP-MS (Agilent model 7700).

8.3. Experimental verification using NTV-ICP-OES with a slow-response CID detector

To evaluate wider applicability of the NTV6 chamber (**Figure 17**), a spectrometer with a CID detector was used. At present, all currently commercially available ICP spectrometers are equipped with an integrating, slow-response detector, either a charge injection device (CID) or a charge coupled device (CCD). By design, integrating detectors cannot acquire data fast enough from transient signals and thus are not well suited for the study of a pressure pulse. The ICP spectrometer with a CID we used was a Thermo Fisher Jarrell Ash Iris (**Figure 20**). This spectrometer can acquire simultaneous data from a max of four wavelengths at a time, with a data acquisition rate of about 40 data points per second. To stretch out (in the time

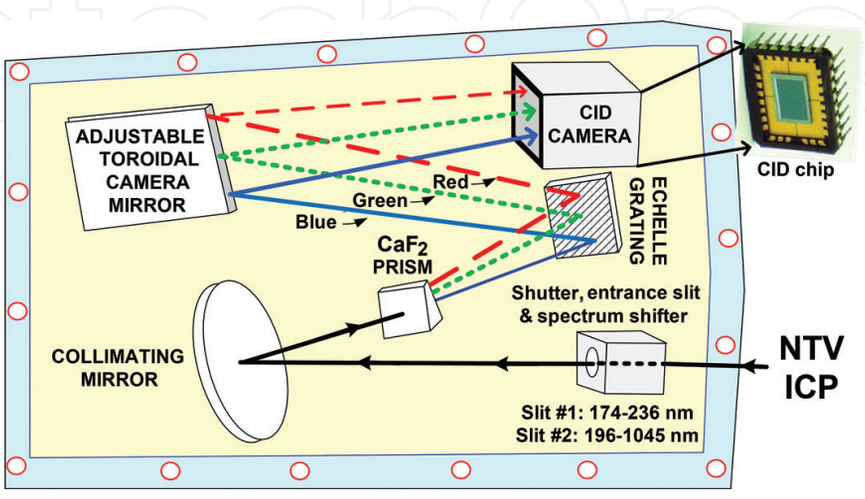

Figure 20. Instrumentation used for validation of chamber design using a spectrometer with a CID detector.

domain) the vaporized "plug" of analyte (and thus acquire signals with more data points), we used relatively lower vaporization powers; thus a measurable pressure pulse was not observed. An example involving Be (Beryllium) monitored using the 313 nm spectral line is shown in **Figure 21**; this is in stark contrast to the Be signal acquired with a PMT detector and shown in **Figure 4d**. Overall, for all elements tested thus far using this system, a pressure pulse was not observed.

8.4. Experimental verification using NTV-ICP-MS: Detection of ions rather than photons

Wider applicability was further demonstrated by interfacing NTV (Chamber NTV6) with an ICP-mass spectrometer (ICP-MS), in this case an Agilent model 7700, thus replacing detection of photons with detection of ions. By design, an ICP-MS of the type shown in **Figure 22a** with a quadrupole mass spectrometer (more accurately, a mass filter) is sequential rather than simultaneous, and it acquires mass-to-charge (m/z) data at a rate of about 10–100 data points per second (depending on manufacturer). Newer-generation ICP-MS systems can acquire thousands (or more) data points per second, and they can provide quasi-simultaneous measurement capabilities (e.g., PerkinElmer NexION 2000). A pressure pulse is not observed when using

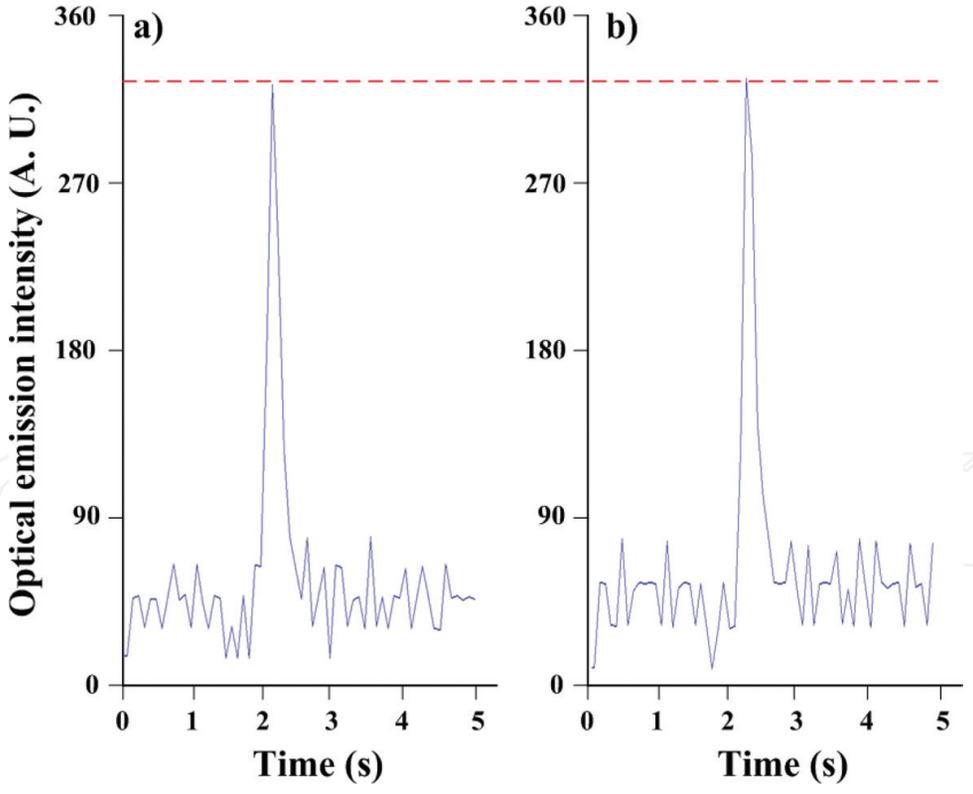

Figure 21. Example signals obtained using NTV and the ICP spectrometer with a CID detector (**Figure 20**). Lack of a pressure pulse at the higher wavelength for Be (at 313 nm) is noteworthy. Also shown is signal-intensity equivalency (per section 2.0 on advantages of NTV), for example, (a) signal obtained from Be by using 1 μL of 10 ppb (part per billion) solution (absolute amount = 10 pg) and (b) signal obtained from 100 μL of 0.1 ppb Be solution (absolute amount = 10 pg) and the same Be 313 nm spectral line. Integration time = 25 ms per data point.

http://dx.doi.org/10.5772/intechopen.72650

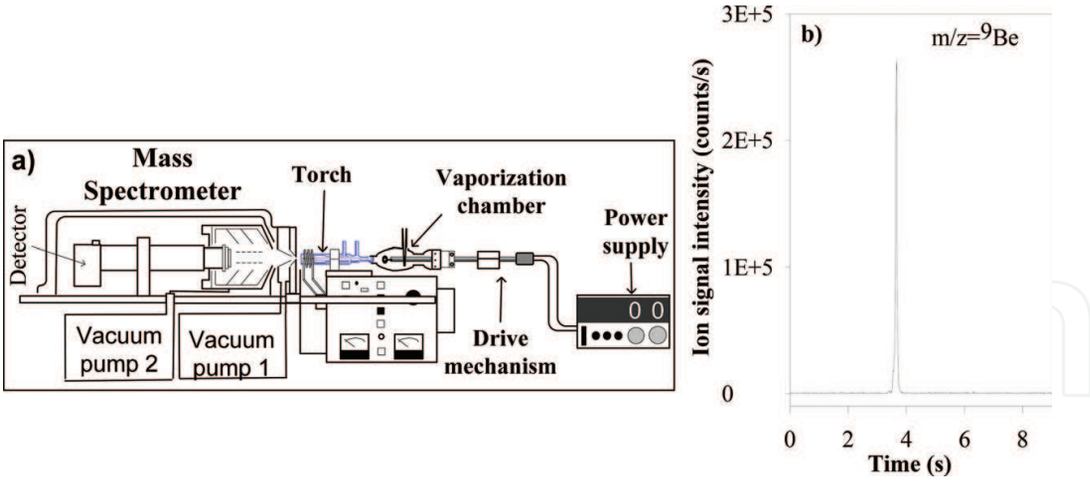

Figure 22. (a) Simplified diagram of ICP-MS. (b) Beryllium (Be) signal demonstrating that there is no pressure pulse when using NTV with ICP-MS.

NTV-ICP-MS because in ICP-MS ions are monitored at specific mass-to-charge ratios, thus making any contribution from plasma background nonexistent. For completeness, ICP-MS is about 1000–10,000 times more sensitive than ICP-OES (primarily due to the very low ICP background observed due to use of a MS). For comparison a signal obtained for Be is shown in **Figure 21b**, and lack of a pressure pulse is noteworthy (**Figure 22b** *versus* **Figure 4d** and **b**).

9. Conclusions drawn by employing ICP systems in a lab

Using smoke visualization experiments and experimentally obtained results by employing an ICP-OES system with a fast-response PMT detector, an ICP-OES system with an integrating (and relatively) slower-response CID detector, and an ICP-MS system, it has been demonstrated that computational fluid dynamics was particularly useful in improving analytical performance characteristics of ICPs. In particular, detection limit improved by a significant factor of ~4. Could similar improvements be obtained using a smaller version of an NTV chamber discussed thus far by coupling it to a portable, battery-operated, small-size microplasma? This question will be briefly addressed next using a rapidly prototyped chamber via 3D printing. 3D printing was selected to reduce costs and time delays when new chambers are needed to be made by the local glassblower.

10. A smaller chamber for microplasmas used in the field

Unlike ICPs discussed thus far that are tethered to a lab floor because they are bulky and heavy and because they require 1–2 kW of electrical power and consume about 20 L/min of expensive Ar gas (**Figure 1**), we have been developing battery-operated microplasmas we made using a variety of technologies ranging from semiconductor fabrication to 3D printing [24–35]. Microplasmas are those with one critical dimension in the micrometer (i.e., sub-mm)

regime. We have been characterizing them [24–35], primarily for "taking part of the lab to the sample" types of applications, i.e., for analytical measurements *on-site*. Future microplasma-based spectrometers are envisioned to have wireless capability [36, 37] and (some) energy autonomy [38–42]. In contrast to ICPs, low gas consumption (e.g., 250 mL/min) and low-power requirements (e.g., ~10 W) are key characteristics of microplasmas. But although low-power operation enables microplasma portability, it also disables liquid sample introduction using a nebulizer (**Figure 1**). The reason is that when using a nebulizer, most of a liquid sample introduced into a microplasma is water. Plasma power required to vaporize the water solvent (introduced with the sample) is 10–30 W [24]. But microplasmas require ~10 W; thus using a nebulizer is not possible. One way of circumventing this is by using a smaller version of the NTV chamber (**Figure 6**). Since a liquid sample is dried prior to its introduction into a microplasma, plasma power is not consumed to vaporize the water solvent, thus enabling liquid micro- or nano-sample introduction into a low-power micoplasma. The instrumentation used is shown in **Figure 23**.

The vaporization chamber used with a microplasma (**Figure 23**) is a scaled-down version of the single-inlet NTV3 chamber (**Figure 17**). Scaling was done assuming that all dimensions (**Table 2**) scale linearly with the "optimum" carrier gas-flow rate of 250 mL/min determined experimentally. A single-inlet chamber was selected to avoid the use of dual mass flow controller (required to ensure balanced flow on both inlets), thus enhancing portability for use *on-site*. To confirm

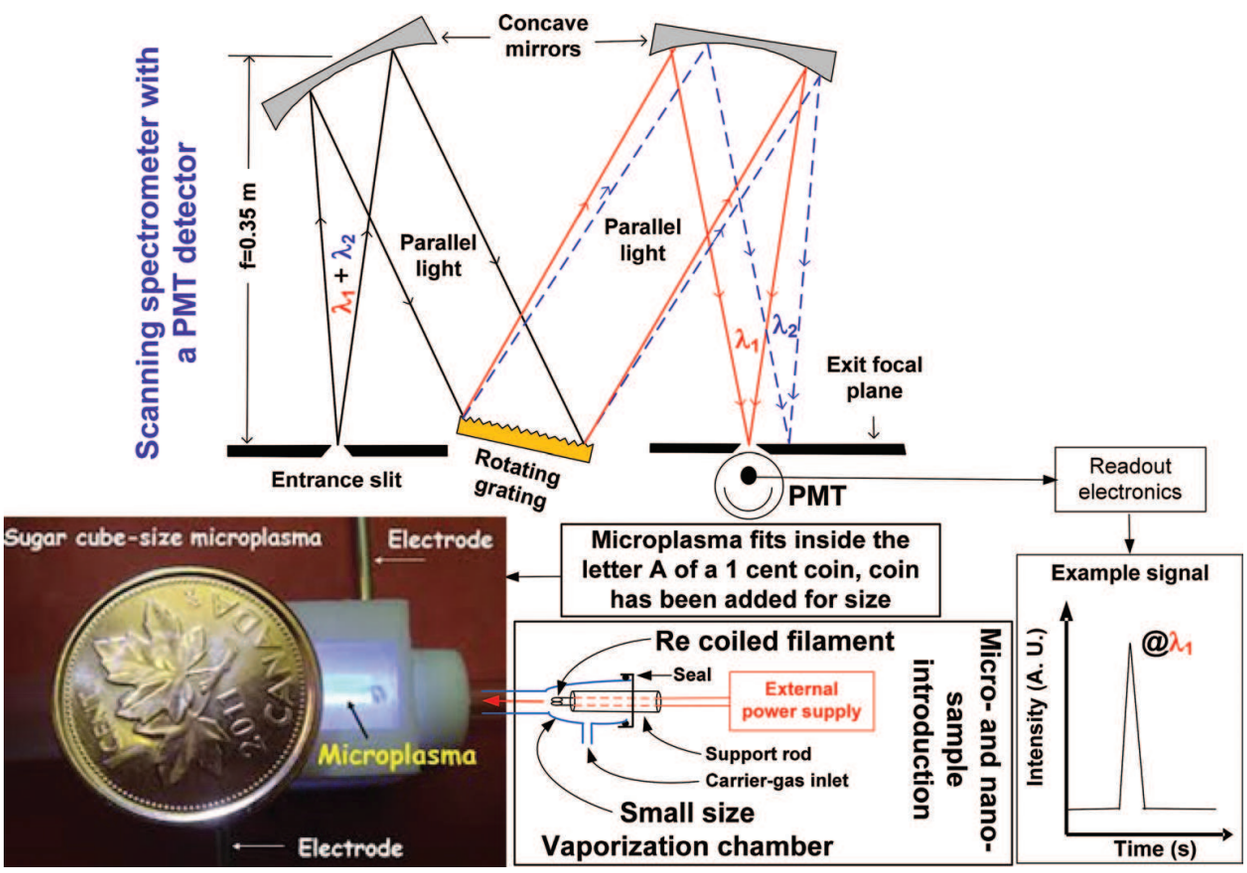

Figure 23. Instrumentation and micro- or nano-sample introduction into a 3D–printed microplasma.

http://dx.doi.org/10.5772/intechopen.72650

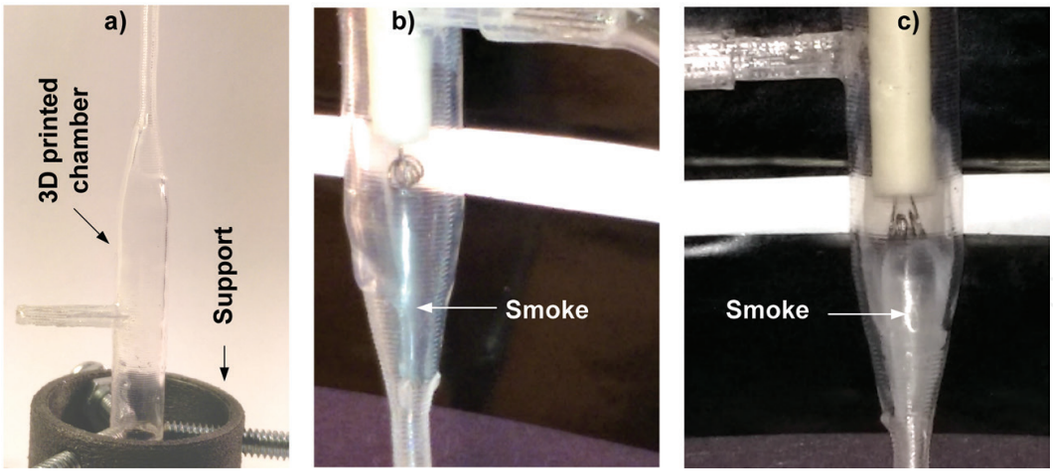

Figure 24. (a) 3D-printed vaporization chamber secured on its drying support. An XTC3D epoxy was used to enhance transparency through the chamber (as required to visually see and record smoke); the support was used to facilitate even drying of the epoxy. (b) Smoke confined to the center of the chamber. The smoke was generated from a drop of gasoline placed on the coil and by gently heating the coil using an external power supply—per **Figure 2a**. (c) Smoke diffused in the chamber (due to the use of an incorrect flow rate).

the scaling assumption and to evaluate flow-rate results, smoke visualization experiments were conducted using a 3D-printed vaporization chamber fabricated from polymeric (e.g., plastic) materials. 3D printing [27–29] was selected to avoid delays caused by the local glassblowing shop and to allow rapid prototyping of candidate chamber designs at a reduced cost. A single frame extracted from videos of smoke visualization experiments is shown in **Figure 24**. Based on these observations, a vaporization chamber has been fabricated using glass and has been used extensively with our microplasmas for measurements by optical emission (**Figure 23**).

11. Overall conclusions

Computational fluid dynamics simulations proved to be highly beneficial for the design of an improved-performance vaporization chamber that was tested with micro- or nano-samples and ICPs installed in a lab. For example, detection limits (a key figure of merit) improved by as much as five times. The best-performing and CFD-simulated chamber was tested with three different ICP spectrometers, thus demonstrating its wider applicability. A scaled-down version of a CFD-simulated NTV chamber has also been used with small-size, portable microplasmas, thus validating scaling-down assumptions and further demonstrating applicability and utility of CFD in plasma spectrometry. Microplasma-based spectrometers are expected to find future applicability for measurements in the field (i.e., *on-site*).

Acknowledgements

Financial assistance from the Natural Sciences and Engineering Research Council (NSERC) of Canada is gratefully acknowledged. A special thank you to Professor (now Emeritus) Cameron

McLeod and his research group at the Department of Chemistry, Sheffield University, UK, for use of their Agilent ICP-MS with our NTV system. A thank you to AEA/CFX of Waterloo, Canada, for a time-limited license to their software.

Author details

Hamid R. Badiei[1,2], Gordon Stubley[3], Ryan Fitzgerald[1], Melanie Saddler[1] and Vassili Karanassios[1]*

*Address all correspondence to: vkaranassios@uwaterloo.ca

1 Department of Chemistry and Waterloo Institute for Nanotechnology, University of Waterloo, Waterloo, Ontario, Canada

2 Perkin Elmer Inc., Ontario, Canada

3 Department of Mechanical and Mechatronics Engineering, University of Waterloo, Waterloo, Ontario, Canada

References

[1] Karanassios V, Grishko V, Reynolds GG. Elemental analysis of micro-samples of liquids or slurries by coiled-filament in-torch vaporization-inductively coupled plasma atomic emission spectrometry (ITV-ICP-AES). Journal of Analytical Atomic Spectrometry. 1999;**14**: 565-570. DOI: 10.1039/A807032F

[2] Badiei HR, Smith AT, Karanassios V. Rhenium-cup, in-torch vaporization (ITV) sample introduction for axially viewed ICP-AES and its application to the analysis of a microscopic, ng-weight solid sample. Journal of Analytical Atomic Spectrometry. 2002;**17**: 1007-1010. DOI: 10.1039/B001781G

[3] Badiei HR, Lai B, Karanassios V. Micro- and nano-volume samples by electrothermal, near-torch vaporization sample introduction using removable, interchangeable and portable rhenium coiled-filament assemblies and axially-viewed inductively coupled plasma-atomic emission spectrometry. Spectrochimica Acta Part B: Atomic Spectroscopy. 2012;**77**:19-30. DOI: 10.1016/j.sab.2012.07.025

[4] Badiei HR, McEnaney J, Karanassios V. Bringing part of the lab to the field: On-site chromium speciation in seawater by electrodeposition of Cr(III)/Cr(VI) on portable coiled-filament assemblies and measurement in the lab by electrothermal, near-torch vaporization sample introduction and inductively coupled plasma-atomic emission spectrometry. Spectrochimica Acta Part B: Atomic Spectroscopy. 2012;**78**:42-49. DOI: 10.1016/j.sab.2012.10.002

[5] Badiei HR, Liu C, Karanassios V. Taking part of the lab to the sample: On-site electrodeposition of Pb followed by measurement in a lab using electrothermal, near-torch vaporization (NTV) sample introduction and inductively coupled plasma-atomic emission spectrometry. Microchemical Journal. 2013;**108**:131-136. DOI: 10.1016/j.microc.2012.10.013

[6] Kantor T. Interpreting some analytical characteristics of thermal dispersion methods used for sample introduction in atomic spectrometry. Spectrochimica Acta Part B: Atomic Spectroscopy. 1988;**43**:1299-1320. DOI: 10.1016/0584-8547(88)80171-X

[7] Kantor T. Electrothermal vaporization and laser ablation sample introduction for flame and plasma spectrometric analysis of solid and solution samples. Spectrochimica Acta Part B: Atomic Spectroscopy. 2001;**56**:1523-1563. DOI: 10.1016/S0584-8547(01)00266-X

[8] Kantor T, Gucerb S. Efficiency of sample introduction into inductively coupled plasma by graphite furnace electrothermal vaporization. Spectrochimica Acta Part B: Atomic Spectroscopy. 1999;**54**:763-772. DOI: 10.1016/S0584-8547(99)00026-9

[9] Grégoire DC, Sturgeon RE. Analyte transport efficiency with electrothermal vaporization inductively coupled plasma mass spectrometry. Spectrochimica Acta Part B: Atomic Spectroscopy. 1999, 1999;**54**:773-786. DOI: 10.1016/S0584-8547(99)00008-7

[10] Ertas G, Holcombe JA. Determination of absolute transport efficiencies of be, cd, in, Pb and bi for electrothermal vaporization sample introduction into an inductively coupled plasma using an in-line electrostatic precipitator. Spectrochimica Acta Part B: Atomic Spectroscopy. 2003;**58**:1597-1612. DOI: 10.1016/S0584-8547(03)00134-4

[11] Piazza R. Thermophoresis: Moving particles with thermal gradients. Soft Matter. 2008; **4**:1740-1744. DOI: 10.1039/B805888C

[12] Braibanti M, Vigolo D, Piazza R. Does thermophoretic mobility depend on particle size? Physical Review Letters. 2008;**100**:108303. DOI: 10.1103/PhysRevLett.100.108303

[13] Zhao C, Cao Z, Fraser J, Oztekin A, Cheng X. Optimization of nanoparticle focusing by coupling thermophoresis and engineered vortex in a microfluidic channel. Journal of Applied Physics. 2017;**121**:024902. DOI: 10.1063/1.4973272

[14] Hoffmann AC, Stein LE. Computational fluid dynamics. In: Gas Cyclones and Swirl Tubes. Berlin: Springer; 2002. DOI: 10.1007/978-3-662-07377-3_7

[15] Ferziger JH, Peric M. Computational Methods for Fluid Dynamics. 3rd ed. Germany: Springer; 2002

[16] Wendt JF, editor. Computational Fluid Dynamics: An Introduction. Germany: Springer; 2008

[17] Chung TJ. Computational Fluid Dynamics. 2nd ed. Cambridge, UK: Cambridge University Press; 2010

[18] Pozrikidis Z. Introduction to Theoretical and Computational Fluid Dynamics. 2nd ed. Oxford, UK: Oxford University Press; 2011

[19] Blazek J. Computational Fluid Dynamics: Principles and Applications. Oxford, UK: Butterworth-Heinemann; 2015

[20] Aref H, Balachandar S. A First Course in Computational Fluid Dynamics. Cambridge, UK: Cambridge University Press; 2017

[21] Badiei HR, Stubley G, Karanassios V. CFD simulation, video clip of a simulation of a single-inlet NTV chamber. November 2017. https://youtu.be/YRooJG_EM4g

[22] Badiei HR, Stubley G, Karanassios V. CFD simulation, video clip of a simulation of a dual-inlet NTV chamber. November 2017. https://youtu.be/FmUawOjIZXM

[23] Badiei HR, Stubley G, Karanassios V. CFD Simulation, Video Clip of Streak-Lines inside a Single-Inlet NTV Chamber. November 2017. https://youtu.be/K4OK8JO3nu4

[24] Karanassios V. Microplasmas for chemical analysis: Analytical tools or research toys? Spectrochimica Acta Part B: Atomic Spectroscopy. 2004;**59**:909-928. DOI: 10.1016/j.sab.2004.04.005

[25] Karanassios V, Johnson K, Smith AT. Micromachined, planar-geometry, atmospheric-pressure, battery-operated microplasma devices (MPDs) on chips for microsamples of liquids, gases or solids by optical emission spectrometry. Analytical and Bioanalytical Chemistry. 2007;**388**:1595-1604. DOI: 10.1007/s00216-007-1273-4

[26] Weagent S, Karanassios V. Helium-hydrogen microplasma device (MPD) on postage-stamp-size plastic-quartz chips. Analytical and Bioanalytical Chemistry. 2009;**395**:577-589. DOI: 10.1007/s00216-009-2942-2

[27] Weagant S, Chen V, Karanassios V. Battery-operated, argon-hydrogen microplasma on hybrid, postage stamp-size plastic-quartz chips for elemental analysis of liquid micro-samples using a portable optical emission spectrometer. Analytical and Bioanalytical Chemistry. 2011;**401**:2865-2880. DOI: 10.1007/s00216-011-5372-x

[28] Weagant S, Li L, Karanassios V. Rapid Prototyping of Hybrid, Plastic-Quartz 3D–Chips for Battery-Operated Microplasmas. London, UK: InTech Publishing; 2011. pp. 1-18 (Chapter 10)

[29] Shatford R, Karanassios V. Microplasma fabrication: from semiconductor technology for 2D–chips and microfluidic channels to rapid prototyping and 3D–printing of microplasma devices. Proceedings of the SPIE. 2014;**9106**:9106H1-9106H7. DOI: 10.11171/12.2050538

[30] Abbaszadeh S, Karim KS, Karanassios V. Measurement of UV from a microplasma by a microfabricated amorphous selenium detector. IEEE Transactions on Electron Devices. 2013;**60**(2):880-883. DOI: 10.1109/TED.2012.2231682

[31] Nguon O, Gauthier M, Karanassios V. Determination of the loading and stability of Pd in an arborescent copolymer in ethanol by microplasma-optical emission spectrometry. RSC Advances. 2014;**4**:8978-8984. DOI: 10.1039/C3RA46232C

[32] Nguon O, Huang S, Gauthier M, Karanassios V. Microplasmas: From applications to fundamentals. Proceedings of SPIE. 2014;**9105**:9101061-9101067. DOI: 10.1117/12.2050348

[33] Weagent S, Dulai G, Li L, Karanassios V. Characterization of rapidly-prototyped, battery-operated, Ar-H_2 microplasma on a chip for elemental analysis of microsamples by portable optical emission spectrometry. Spectrochimica Acta Part B: Atomic Spectroscopy. 2015;**106**:75-80. DOI: 10.1016/j.sab.2015.01.009

[34] Weagant S, Karanassios V. Battery-operated, planar-geometry microplasma on a post-age-stamp size chips: Some fundamentals. Proceedings of SPIE. 2011;**8024**:80240L. DOI: 10.1117/12.884329

[35] Weagant S, Smith AT, Karanassios V. Mobile micro- and Nano-instruments: Small, cheap and under wireless control. ECS Transactions. 2010;**28**(14):1-6. DOI: 10.1149/1.3490180

[36] Trzcinski P, Weagent S, Karanassios V. Wireless data acquisition of transient signals for mobile spectrometry applications. Applied Spectroscopy. 2016;**70**:905-915. DOI: 10.1177/0003702816638304

[37] Trzcinski P, Karanassios V. How can wireless, mobile data acquisition be used for taking part of the lab to the sample, and how can it join the internet of things? Proceedings of SPIE. 2016;**9855**:985503. DOI: 10.1117/12.2224400

[38] Abbaszadeh S, Karim KS, Karanassios V. A microfabricated, low dark current a-se detector for measurement of microplasma optical emission in the UV for possible use on-site. Proceedings of SPIE. 2013;**8726**:87260S. DOI: 10.1109/TED.2012.2231682

[39] Zhang X, Karanassios V. Rapid prototyping of solar-powered, battery-operated, atmospheric-pressure, sugar-cube size microplasma on hybrid, 3D chips using a portable optical emission spectrometer. Proceedings of SPIE. 2012;**8366**:83660D. DOI: 10.1117/12.919550

[40] Shatford R, Karanassios V. 3D printing in chemistry: Past, present and future. Proceedings of SPIE. 2016;**9855**:98550B-998560. DOI: 10.1117/12.2224404

[41] Lee D, Dulai G, Karanassios V. Survey of energy harvesting and energy scavenging approaches for on-site powering of wireless sensor- and microinstrument-networks. Proceedings of SPIE. 2013;**8028**:8720S1. DOI: 10.1117/12.2016238

[42] Trizcinski P, Nathan A, Karanassios V. Approaches to energy harvesting and energy scavenging for energy autonomous sensors and microinstruments. Proceedings of SPIE. 2017;**10194**:10194A1-10194A9. DOI: 10.1117/12.2262957

IntechOpen